Origin of discrepancy between electrical and mechanical anomalies in lead-free (K,Na)NbO_3-based ceramics

A. M. Mazuera,* P. S. Silva, Jr., A. D. Rodrigues, P. S. Pizani, Y. Romaguera-Barcelay, and M. Venet
Department of Physics, Federal University of São Carlos, CP-676, São Carlos, São Paulo, Brazil

M. Algueró
Instituto de Ciencia de Materiales de Madrid, CSIC, Cantoblanco 28049 Madrid, Spain
(Received 22 March 2016; revised manuscript received 21 September 2016; published 7 November 2016)

Ferroelectric polymorphic phase coexistence, associated with either the presence of a morphotropic phase boundary or a temperature-driven polymorphic phase transition, is currently acknowledged as the key to high piezoelectric activity and is searched when new perovskite materials are developed, like lead-free alternatives to state-of-the-art Pb(Zr,Ti)O_3. This requires characterization tools that allow phase coexistence and transitions to be readily identified, among which measurements of the temperature dependences of Young's modulus and mechanical losses by dynamical mechanical analysis stand out as a powerful technique to complement standard electrical characterizations. We report here the application of this technique to ($K_{1-x}Na_x$)NbO_3-based materials, which are under extensive investigation as environmentally friendly high sensitivity piezoelectrics. The elastic anomalies associated with the different phase transitions are identified and are shown to be distinctively shifted in relation to the dielectric ones. The origin of this discrepancy is discussed with the help of temperature-dependent Raman spectroscopy and is proposed to be a characteristic of diffuse phase transitions.

DOI: 10.1103/PhysRevB.94.184101

I. INTRODUCTION

Piezoelectric ceramics are widely used in a range of technologies as active elements in high-performance devices, such as ultrasound transducers, different sensors, actuators and smart systems, and energy harvesters to name a few examples [1,2]. Lead zirconate titanate (PZT) ceramics are mostly used for these applications. However, the lead content in PZT materials has raised environmental concerns, and recent governmental regulations require their replacement by environmentally friendly alternatives [3]. Consequently, research is intensive in the search for alternative lead-free materials with comparable performance, among which $BaTiO_3$ (BT), $Bi_{0.5}Na_{0.5}TiO_3$ (BNT), and (K,Na)NbO_3 (KNN) based compositions stand out [4–6].

A promising candidate for substituting PZT is potassium sodium niobate, specifically, chemically tailored compositions for enhanced response [7]. The ($K_{1-x}Na_x$)NbO_3 perovskite solid solution shows a morphotropic phase boundary (MPB) between two orthorhombic polymorphs at $x = 0.5$. In addition, compositions around this MPB undergo two successive polymorphic phase transitions (PPT) on heating, first to a tetragonal phase at 225 °C and then to a cubic phase, actually the ferroelectric phase transition at a Curie temperature of 435 °C [8]. Large piezoelectric responses are obtained at the low-temperature PPT.

Indeed, KNN modifications initially aimed at decreasing the temperature of the PPT, until locating it close to room temperature (RT). High piezoelectric coefficients were obtained with this strategy which were further increased by ceramics texturing [9]. Nevertheless, poor thermal stability results, and subsequent efforts have concentrated on engineering actual MPBs in KNN, instead of moving the PPT down to RT [10].

It is widely accepted now that ferroelectric polymorphic phase coexistence, associated with either the existence of a morphotropic phase boundary or a temperature-driven polymorphic phase transition, is the key to high piezoelectric activity and must be searched when new compositions are designed [11]. This requires characterization tools that allow the phase coexistence and associated phase transitions to be readily identified before in-depth structural studies are carried out.

Measurements of the dielectric permittivity as a function of temperature have traditionally played this role; for phase transitions, both the ferroelectric transition and low-temperature polymorphic ones have associated distinctive dielectric anomalies. However, conductivity is often an issue that can complicate their identification. Also, chemical disorder originating from multiple occupancy of one lattice site can result in the appearance of relaxor states, which also have associated characteristic dielectric maxima [12]. In these cases, measurements of the temperature dependence of the low-frequency Young's modulus by dynamical mechanical analysis (DMA) have been shown to nicely complement electrical measurements and to enable identifying the phase transitions for a number of complicated examples [13–15].

The technique provides not only the Young's modulus but also internal friction, which reflect the dynamics of point and extended defects like the ferroelectric/ferroelastic domain walls [16–19]. We report here the application of DMA to the study of KNN-based materials. Emphasis is put on the analysis of the origin of some unexpected discrepancies between the phase transition temperatures determined from the electrical and mechanical results, which are discussed with the help of temperature-dependent Raman spectroscopy. The generality of the described phenomenology

*anmazuera@df.ufscar.br

for perovskite systems showing diffuse phase transitions is highlighted.

II. EXPERIMENTAL DETAILS

The perovskite oxide with the composition $(K_{0.5}Na_{0.5})_{0.97}Li_{0.03}Nb_{0.8}Ta_{0.2}O_3$, abbreviated as KNLNT, was selected as a model system of KNN-based materials. This is one of the two compositions pointed out in Ref. [9] (referred to there as LF3) as a viable alternative to replace PZT-based materials. Perovskite powders were prepared by the conventional mixed-oxide method. Stoichiometric mixtures of high-purity K_2CO_3, Na_2CO_3, Li_2CO_3, Nb_2O_5, and Ta_2O_5 were initially homogenized by ball milling in isopropyl alcohol for 24 h and dried. A calcination step was then carried out at 850 °C for 5 h to obtain the desired phase.

Ceramic samples were processed also by conventional means. The calcined powder was milled, dried, and mixed with 3 wt % polyvinyl butyral (PVB) as a binder. Green disks with a 7-mm diameter were then obtained by uniaxial pressing at 150 MPa and further consolidated by cold-isostatic pressing at 300 MPa. Sintering was carried out at 1050 °C for 2 h in closed crucibles in the presence of KNLNT sacrificial powder. These are standard procedures for the processing of KNN-based ceramics [20], which consistently lead to densities around 4.70 g cm^{-3} as determined with Archimedes's method. This corresponds to a densification of 95%.

Final phases in the ceramics were monitored by x-ray diffraction (XRD) with a LabX XRD-6000 Shimadzu apparatus. A typical XRD pattern is shown in Fig. 1(a). The desired perovskite structure was obtained without traces of spurious phases. All peaks can be indexed according to Inorganic Crystal Structure Database (ICSD) Collection Code 185533, corresponding to the space group $Bmm2$. The expected orthorhombic phase is thus found, with a negligible percentage of tetragonal phase. Note the distinctive splitting of the (010) and (020) peaks of the parent cubic phase, expanded in Fig. 1(b) [21,22].

Microstructure was characterized by scanning electron microscopy (SEM) with a JEOL 5400 LV apparatus. Figure 2 shows an image of the $(K_{0.5}Na_{0.5})_{0.97}Li_{0.03}Nb_{0.8}Ta_{0.2}O_3$ ceramic. A dense microstructure with a low porosity level can be observed, which is in agreement with the high densification achieved. Grain size was measured using the intercept method,

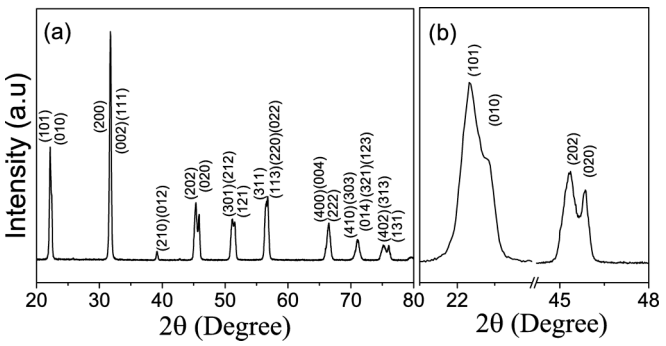

FIG. 1. X-ray diffraction pattern of a $(K_{0.5}Na_{0.5})_{0.97}Li_{0.03}Nb_{0.8}Ta_{0.2}O_3$ ceramic. Miller indexes correspond to those of the orthorhombic perovskite (space group $Bmm2$).

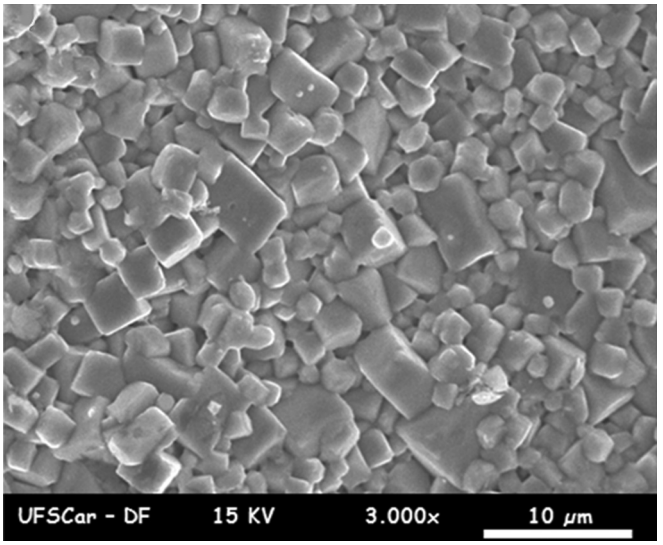

FIG. 2. Microstructure of the $(K_{0.5}Na_{0.5})_{0.97}Li_{0.03}Nb_{0.8}Ta_{0.2}O_3$ ceramic.

and an average value of 2.7 μm was obtained, which is large enough to have no influence on the diffuse character of the transition [23].

Test ceramic capacitors were processed for the electrical characterization by painting silver electrodes on both sides of the sintered disks and annealing them at 590 °C for 1 h. This involved measuring the temperature dependence of the dielectric permittivity and losses at several frequencies between 100 Hz and 1 MHz from RT up to 400 °C by using an IET 7600 plus high-precision LCR meter.

Ceramic bars with dimensions of 25.0 × 6.7 × 1.0 mm were machined out of the disks for mechanical characterization by dynamic mechanical analysis in the three-point bending configuration. A DMA8000 PerkinElmer apparatus was used. This technique provides the dynamic Young's modulus Y, and thus the elastic compliance, as a function of frequency and temperature, along with the internal friction Q^{-1}. Basically, one measures the amplitude and phase relationships between the input (force) and output (displacement) waves, from which Y and Q^{-1}, often also referred to as the mechanical losses, are obtained. Measurements between RT and 400 °C at 1, 5, and 10 Hz were carried out.

Additionally, in order to support our discussions, the evolution with temperature of the perovskite crystalline structure was studied by micro-Raman spectroscopy using a Horiba Jobin Yvon LabRam HR Evolution spectrometer, combined with a Linkam THS 1500 hot stage. The 632-nm line of a He-Ne laser was used for excitation, with the power kept below 1 mW to avoid undesirable heating effects. The adopted experimental configurations correspond to a spectral resolution of 1.5 cm^{-1}. Data were taken in the same temperature range in which the electrical and mechanical characterizations were carried out. Spectra were normalized, after which the parameters of the identified Raman modes were obtained using IGOR software from the best fit to a sum of damped oscillator functions according to the formula [24,25]

$$I(\omega,T)=[1+n(\omega,T)]\sum_{i=1}^{N}A_{Oi}\frac{\omega\Omega_{Oi}^2\Gamma_{Oi}^2}{\left(\Omega_{Oi}^2-\omega^2\right)^2+\omega^2\Gamma_{Oi}^2}, \quad (1)$$

where $I(\omega,T)$ is the Raman intensity, $n(\omega,T)$ is the Bose-Einstein factor, A_{0i} is the oscillator strength, Ω_{Oi} is the wave number, and Γ_{Oi} is the damping factor of the ith oscillator.

III. RESULTS AND DISCUSSION

The temperature dependence of the dielectric permittivity and losses of a KNLNT ceramic is shown in Fig. 3 at 1, 10, and 100 kHz. Thermal hysteresis was barely found, so only curves on heating are included. The dielectric anomaly associated with the ferroelectric transition is clearly observed with maximum permittivity at 342 °C. Dielectric losses also showed a maximum at a slightly lower temperature (~339 °C), above which they exponentially increased, reflecting the high-temperature conductivity. Additionally, there is a second small dielectric anomaly at ~86 °C that has been related to the orthorhombic-tetragonal transition.

The temperature dependence of the low-frequency Young's modulus and internal friction of an analogous KNLNT sample are also shown in Fig. 3. The elastic anomaly associated with the ferroelectric transition is also clearly seen with a minimum Young's modulus at 305 °C. Internal friction, which is thought to reflect the presence of dynamic ferroelectric/ferroelastic domain walls, peaks at 280 °C, above which it readily decreases until becoming negligible at 330 °C. There is also a second small elastic anomaly at ~60 °C that has an associated steplike decrease of internal friction.

There is thus a distinctive difference between the temperatures of the main dielectric and elastic anomalies, which are both thought to be associated with the ferroelectric phase transition. Moreover, there is a similar discrepancy between the temperatures of the second low-temperature dielectric and elastic anomalies that have been proposed to be related to the orthorhombic-tetragonal PPT. Although this discrepancy has not been observed in model ferroelectrics, such as perovskite $BaTiO_3$ [26], it has been noticed in

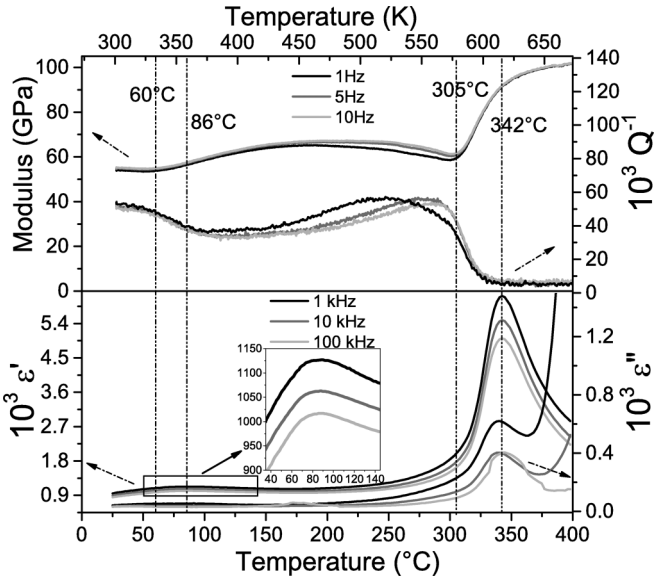

FIG. 3. Temperature dependences of (top) Young's modulus and internal friction Q^{-1} and (bottom) dielectric permittivity ε' and losses ε'' for a KNLNT ceramic sample.

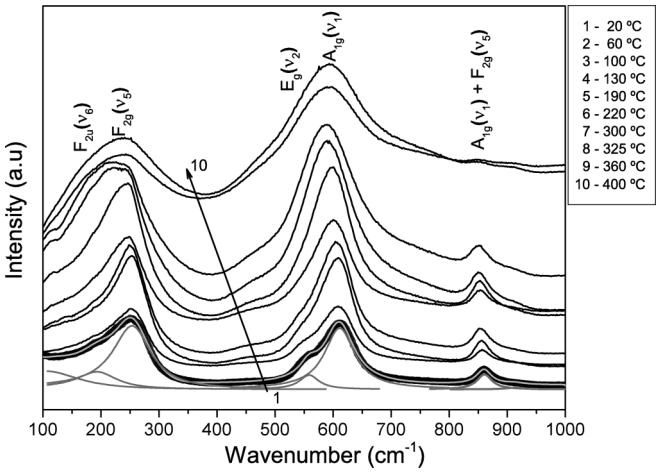

FIG. 4. Normalized Raman spectra, corrected for the Bose-Einstein factor, at increasing temperatures between 20 °C and 400 °C for a KNLNT ceramic. Gray lines represent the decomposition of the spectrum at 20 °C from the best fit of Eq. (1).

doped materials and solid solutions that have diffuse phase transitions, that is, that undergo the ferroelectric transition across a wide temperature range, such as commercial ferroelectric PZT5H and PZT8 ceramics [27] and antiferroelectric (Pb,Ba,La)(Zr,Ti,Sn)O_3 [27], and also in the relaxor ferroelectric system $Pb(Mg_{1/3}Nb_{2/3})O_3$-$PbTiO_3$ [28,29]. The origin of this phenomenology was further studied with the help of Raman spectroscopy.

Spectra for a KNLNT ceramic at increasing temperatures are shown in Fig. 4, where the spectral decomposition at 20 °C is also depicted. Note that the Raman data are corrected for the Bose-Einstein thermal factor:

$$R(\omega) = \frac{S(\omega)}{[1+n(\omega)]} = \frac{S(\omega)}{\left[1-e^{\left(-\frac{\hbar\omega}{\kappa_B T}\right)}\right]^{-1}}, \qquad (2)$$

where $R(\omega)$ is the reduced Raman data for the Bose-Einstein thermal factor, $S(\omega)$ is the measured Raman intensity, and $\hbar$ and κ_B are Planck's and Boltzmann's constants, respectively.

We will discuss the three observed regions at ~250, ~600, and 860 cm^{-1}, which correspond to different vibrational modes of the NbO_6 octahedron and directly reflect the phase transitions [30–32]. The Raman bands consist of five vibrational modes; the intermediate wave-number modes, $A_{1g}(\nu 1)$ (~615 cm^{-1}) and $E_g(\nu 2)$ (~555 cm^{-1}), are associated with O-Nb-O bond stretching modes, while low- and high-wave-number modes, $F_{2u}(\nu 6)$ (~200 cm^{-1}), $F_{2g}(\nu 5)$ (~260 cm^{-1}), and the combination of $A_{1g}(\nu 1)$ plus $F_{2g}(\nu 5)$ (~860 cm^{-1}), are related to O-Nb-O bending modes [31,33–36]. The evolution of the position of peaks $F_{2u}(\nu 6)$, $F_{2g}(\nu 5)$, $E_g(\nu 2)$, $A_{1g}(\nu 1)$, and $A_{1g}(\nu 1) + F_{2g}(\nu 5)$ with temperature is shown in Fig. 5(a). As can be noticed, peak wave numbers vary nonmonotonically with temperature with distinctive changes of slope at specific points. Temperature-induced shifts can be attributed to the intensification of anharmonic effects in which a zone-center optical phonon decays to an acoustic phonon having momenta with equal magnitude and opposite direction [37]. The temperature dependence of the central

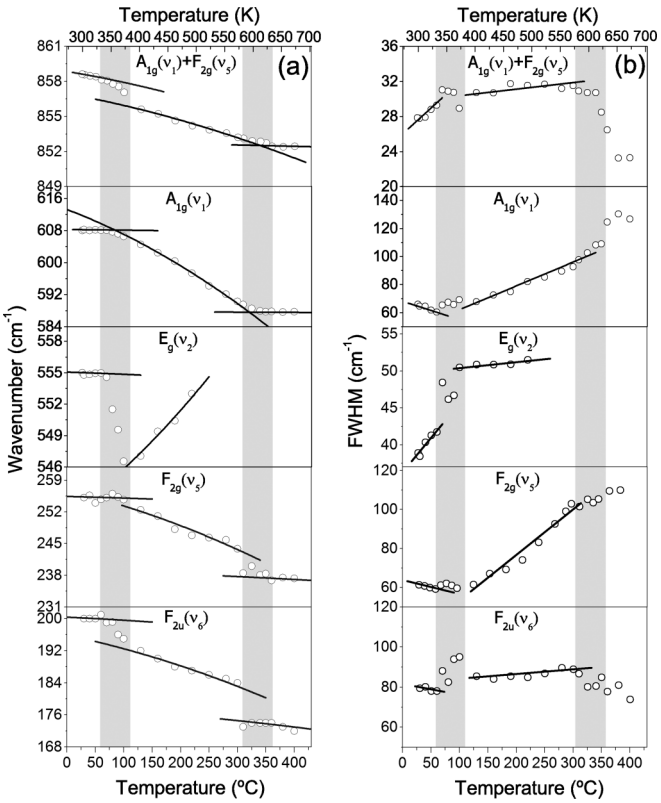

FIG. 5. Temperature dependences of (a) wave numbers and (b) FWHM for the $F_{2u}(\nu 6)$, $F_{2g}(\nu 5)$, $A_{1g}(\nu 1) + F_{2g}(\nu 5)$, $A_{1g}(\nu 1)$, and $E_g(\nu 2)$ modes.

position of the peak $\omega(T)$ is given by the monotonic function

$$\omega(T) = \omega_0 + A\left[1 + \frac{2}{e^{\frac{\hbar\omega_0}{2\kappa_B T}} - 1}\right] + B\left[1 + \frac{3}{e^{\frac{\hbar\omega_0}{3\kappa_B T}} - 1} + \frac{3}{\left(e^{\frac{\hbar\omega_0}{3\kappa_B T}} - 1\right)^2}\right], \quad (3)$$

where ω_0, A, and B are constants depending on the decay processes involving four phonons.

For values slightly above the room temperature, the evolutions of the central position of the five peaks are in good agreement with Eq. (3). The anharmonic parameters of the five curves in this temperature range are specified in Table I. For temperatures higher than 60 °C, the peaks no longer follow Eq. (3). When the temperature is further increased, peaks present drastic deviations (shaded area), as mainly evidenced by abrupt reductions in the wave numbers of $E_g(\nu 2)$, $A_{1g}(\nu 1) + F_{2g}(\nu 5)$, and $F_{2u}(\nu 6)$. For temperatures higher than 100 °C, peak evolutions are again well described by temperature-induced anharmonic effects. The distinct anharmonicity of the modes in comparison with those of the first interval, which is measured by the different anharmonic coefficients, evidences the existence of different structures in the two ranges. Anomalies in the peak positions take place again for temperatures higher than 300 °C, marked as a second shaded area. When the heating exceeds 360 °C, peaks again follow the thermal anharmonic shifts, in this case presenting weaker anharmonicities than those for the two previous structures, indicating the transition to another symmetry. The behavior of the damping of the vibrational modes also presents anomalies for the same temperature ranges. In Fig. 5(b), the FWHM evolutions, illustrated by lines, have deviations in shaded areas, confirming the transitional character in these regions.

As can be observed in Fig. 6, the integral intensity of the $A_{1g}(\nu 1) + F_{2g}(\nu 5)$ peak also shows a distinctive evolution, characterized by a moderate increase from ∼60 °C and a fast decrease above 300 °C, until basically disappearing at ∼360 °C. This mode is characteristic of the polar phases, and the steps are associated with the successive PPT on heating.

It is worth noting that the temperature at which the mode vanishes (∼360 °C) is the same one from which the reciprocal permittivity starts following the Curie-Weiss law on heating, as shown in Fig. 7. The Curie-Weiss law holds in the high-temperature paraelectric phase, and the deviation of the permittivity from it on cooling is usually interpreted as the onset of the ferroelectric transition (the appearance of the first ferroelectric precursors). Likewise, this temperature can be considered that at which the ferroelectric phase has completely disappeared on heating, in agreement with the right side of the second shaded area in Fig. 5. Following the argument, the temperature corresponding to the left side of the shaded area would be that at which the ferroelectric phase starts transforming into the paraelectric one (when the first cubic precursors nucleate). This is 300 °C and roughly coincides with the temperature of the elastic anomaly.

The reason why the elastic anomaly signals the onset of the ferroelectric to cubic transition instead of the average

TABLE I. Anharmonic parameters for the vibrational modes $A_{1g}(\nu 1) + F_{2g}(\nu 5)$, $A_{1g}(\nu 1)$, $E_g(\nu 2)$, $F_{2g}(\nu 5)$, and $F_{2u}(\nu 6)$ in three temperature ranges.

	Temperature range (°C)								
	26–60			110–300			360–400		
	ω_0 (cm^{-1})	A (cm^{-1})	B (cm^{-1})	ω_0 (cm^{-1})	A (cm^{-1})	B (cm^{-1})	ω_0 (cm^{-1})	A (cm^{-1})	B (cm^{-1})
$A_{1g}(\nu 1) + F_{2g}(\nu 5)$	861.5	−1.35	−0.55	859.8	−1.45	−0.59	853.1	−0.15	−0.03
$A_{1g}(\nu 1)$	608.5	−0.10	−0.05	625.2	−3.6	−2.27	587.7	−0.03	−0.01
$E_g(\nu 2)$	555.5	−0.17	−0.05	533.9	1.75	1.25			
$F_{2g}(\nu 5)$	256.0	−0.10	−0.02	262.0	−0.65	−0.23	239.5	−0.04	−0.02
$F_{2u}(\nu 6)$	201.5	−0.11	−0.03	201.0	−0.52	−0.13	179.0	−0.05	−0.03

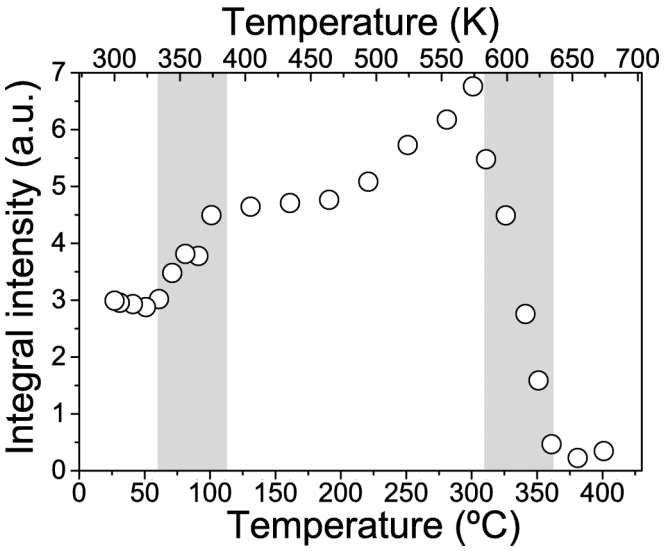

FIG. 6. Temperature dependence of the integral intensity for the $A_{1g}(\nu 1) + F_{2g}(\nu 5)$ mode.

transition must be the sensitivity of Young's modulus to the ferroelectric/ferroelastic activity. Indeed, thermodynamic theory predicts a step [38] and not a minimum in Young's modulus that is thus associated with a maximum of the ferroelastic contribution (domain wall density and mobility are known to be enhanced at the brink of the transition). Note that the maximum of the internal friction occurs at a slightly lower temperature, indicating maximum energy dissipation preceding the onset of the ferroelectric to paraelectric transition. On the contrary, the dielectric anomaly at 342 °C signals the average transition, at which half the tetragonal phase has transformed into the cubic one, coinciding with the center of the second shaded area in Fig. 5.

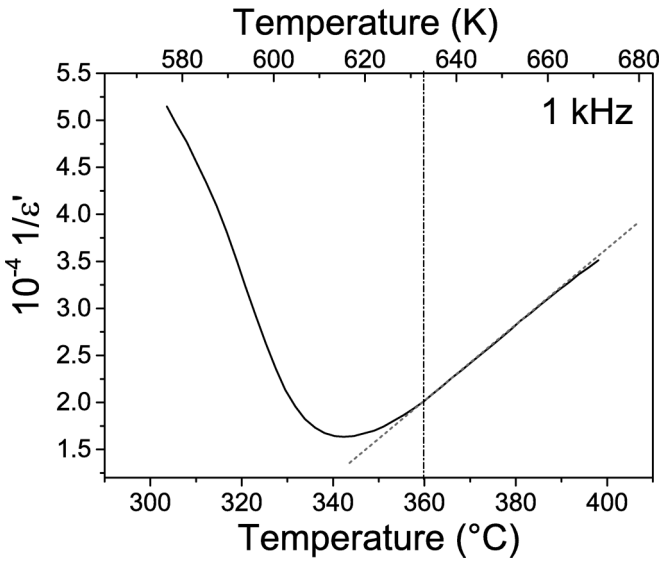

FIG. 7. Temperature dependence of the reciprocal dielectric permittivity of a KNLNT ceramic at 1 KHz. The Curie-Weiss regime and the temperature from which the data deviate are indicated by straight lines.

The low-temperature anomalies in Raman data are related to the PPT transition. Changes in phonon energies far from regular anharmonic shifts can only be due to atomic rearrangements associated with structural transitions. The left side of first shaded area indicates the temperature limit for the exclusive existence of a homogeneous orthorhombic structure. This is also the temperature of the elastic anomaly that would indicate again the onset of the transition, which is very diffuse in this case. Similarly, the dielectric anomaly at 80 °C–90 °C signals the average transition. Indeed, the $E_g(\nu 2)$ mode has been reported to be characteristic of the orthorhombic phase [31,39,40], and thus, its disappearance at ∼200 °C can be considered its completion.

Note that this phenomenology is a consequence of the phase transitions taking place in a broad temperature range, i.e., having a diffuse character, in systems ferroelastically active like KNLNT. Indeed, a similar discrepancy between the positions of the dielectric and elastic anomalies associated with the ferroelectric transition has been described for Nb-doped PZT with a highly diffuse phase transition (and enhanced ferroelectric/ferroelastic domain wall activity) [41]. Basically, one can conclude that in systems with diffuse transition, the elastic anomaly indicates the onset of the ferroelectric to cubic transition on heating (and the completion of the ferroelectric transition on cooling), while the dielectric anomaly indicates the average transition temperature. The difference thus is a direct measurement of the diffuseness of the transition.

It is worth mentioning that diffuse phase transitions are a quite general phenomenon in ferroelectric systems, which not only appear as a consequence of chemical disorder in one or both perovskite sites but also result from nanostructuring, as described for $BaTiO_3$ [23]. Therefore, the phenomenology presented and comprehensively discussed here is relevant not only for the design and development of novel perovskite solid solutions, such as those lead-free high-sensitivity piezoelectrics and multiferroic magnetoelectrics under extensive investigation [10,11,42], but also for the downscaling of ferroelectric ceramic technologies like multilayer ceramic actuators [43].

IV. CONCLUSIONS

The temperature dependences of the low-frequency Young's modulus and internal friction of $(K_{0.5}Na_{0.5})_{0.97}Li_{0.03}Nb_{0.8}Ta_{0.2}O_3$ ceramics have been measured by dynamical mechanical analysis across the orthorhombic-tetragonal and tetragonal-cubic polymorphic phase transitions, that is, the low-temperature PPT and ferroelectric transition of the system. Distinctive elastic anomalies take place at both transitions but at temperatures lower than the corresponding electric anomalies found in the temperature dependence of the dielectric permittivity. The origin of this discrepancy has been studied with the help of temperature-dependent Raman spectroscopy. Results clearly indicate the elastic anomalies signal the onset of the polymorphic transitions on heating (or their completion on cooling), while the dielectric anomalies take place at the average temperature. This is a consequence of a main contribution of ferroelastic domain dynamics to Young's modulus, which does not dominate permittivity,

and a characteristic of diffuse phase transitions. Indeed, the difference in temperature between the elastic and dielectric anomalies is a measurement of the diffuseness of the phase transition. The technique can be effectively used then in the search for novel lead-free perovskite systems with morphotropic phase boundaries or polymorphic phase transitions and high piezoelectric response.

ACKNOWLEDGMENTS

The authors would like to thank CAPES and the São Paulo Research Foundation (FAPESP), Grants No. 2012/08457-7 and No. 2013/00134-7, for the financial support. M.A. also acknowledges funding from MINECO through the MAT2014-58816-R Project.

[1] N. Setter, in *Piezoelectric Materials in Devices: Extended Reviews on Current and Emerging Piezoelectric Materials, Technology, and Applications* (Ecole polytechnique federale de Lausanne, Lausanne, Switzerland, 2002), p. 518.
[2] S. R. Anton and H. A. Sodano, Smart Mater. Struct. **16**, R1 (2007).
[3] J. Rödel, W. Jo, K. T. P. Seifert, E.-M. Anton, T. Granzow, and D. Damjanovic, J. Am. Ceram. Soc. **92**, 1153 (2009).
[4] T. R. Shrout and S. Zhang, J. Electroceram. **19**, 185 (2007).
[5] W. Liu and X. Ren, Phys. Rev. Lett. **103**, 257602 (2009).
[6] A. Moosavi, M. A. Bahrevar, A. R. Aghaei, P. Ramos, M. Algueró, and H. Amorín, J. Phys. D **47**, 055304 (2014).
[7] J.-F. Li, K. Wang, F.-Y. Zhu, L.-Q. Cheng, and F.-Z. Yao, J. Am. Ceram. Soc. **96**, 3677 (2013).
[8] B. Jaffe, H. Jaffe, and W. Cook, in *Piezoelectric Ceramics*, Non-metallic Solids, Vol. 3 (Academic Press, London, 1971), p. 317.
[9] Y. Saito, H. Takao, T. Tani, T. Nonoyama, K. Takatori, T. Homma, T. Nagaya, and M. Nakamura, Nature (London) **432**, 84 (2004).
[10] X. Wang, J. Wu, D. Xiao, J. Zhu, X. Cheng, T. Zheng, B. Zhang, X. Lou, and X. Wang, J. Am. Chem. Soc. **136**, 2905 (2014).
[11] J. Wu, D. Xiao, and J. Zhu, Chem. Rev. **115**, 2559 (2015).
[12] L. Martín-Arias, A. Castro, and M. Algueró, J. Mater. Sci. **47**, 3729 (2012).
[13] F. Cordero, Materials **8**, 8195 (2015).
[14] M. Algueró, B. Jiménez, and L. Pardo, Appl. Phys. Lett. **87**, 082910 (2005).
[15] H. Amorín, R. Jiménez, E. Vila, M. Dollé, A. Castro, and M. Algueró, Phase Trans. **86**, 681 (2013).
[16] F. Cordero, Phys. Rev. B **76**, 172106 (2007).
[17] F. Cordero, H. T. Langhammer, T. Müller, V. Buscaglia, and P. Nanni, Phys. Rev. B **93**, 064111 (2016).
[18] M. Algueró, B. Jiménez, and L. Pardo, Appl. Phys. Lett. **83**, 2641 (2003).
[19] M. Algueró, R. Jiménez, H. Amorín, E. Vila, and A. Castro, Appl. Phys. Lett. **98**, 202904 (2011).
[20] M. Matsubara, T. Yamaguchi, W. Sakamoto, K. Kikuta, T. Yogo, and S.-i. Hirano, J. Am. Ceram. Soc. **88**, 1190 (2005).
[21] Y. Inagaki, K.-i. Kakimoto, and I. Kagomiya, J. Am. Ceram. Soc. **93**, 4061 (2010).
[22] N. Ishizawa, J. Wang, T. Sakakura, Y. Inagaki, and K. Kakimoto, J. Solid State Chem. **183**, 2731 (2010).
[23] Y. Park, W.-J. Lee, and H.-G. Kim, J. Phys.: Condens. Matter **9**, 9445 (1997).
[24] G. Burns and B. A. Scott, Phys. Rev. B **7**, 3088 (1973).
[25] E. Buixaderas, D. Nuzhnyy, I. Gregora, S. Kamba, M. Berta, B. Malič, and M. Kosec, IEEE Trans. Sonics Ultrason. **56**, 1843 (2009).
[26] B. L. Cheng, M. Gabbay, M. Maglione, and G. Fantozzi, J. Electroceram. **10**, 5 (2003).
[27] C. Wu, X. Wang, and X. Yao, Ceram. Int. **38**(Suppl. 1), S13 (2012).
[28] F. Cordero, F. Craciun, and P. Verardi, Ferroelectrics **290**, 141 (2003).
[29] R. Jiménez, H. Amorín, J. Ricote, J. Carreaud, J. M. Kiat, B. Dkhil, J. Holc, M. Kosec, and M. Algueró, Phys. Rev. B **78**, 094103 (2008).
[30] Y. Dai, X. Zhang, and G. Zhou, Appl. Phys. Lett. **90**, 262903 (2007).
[31] W. L. Zhu, J. L. Zhu, Y. Meng, M. S. Wang, B. Zhu, X. H. Zhu, J. G. Zhu, D. Q. Xiao, and G. Pezzotti, J. Phys. D **44**, 505303 (2011).
[32] M. Połomska, B. Hilczer, M. Kosec, and B. Malič, Ferroelectrics **369**, 149 (2008).
[33] Y. Hu, H. Gu, and Z. Wang, in *Nanowires: Fundamental Research*, edited by A. Hashim (INTECH Open Access Publisher, Rijeka, Croatia, 2011), Chap. 7.
[34] Y. Chang, Z.-p. Yang, D. Ma, Z. Liu, and Z. Wang, J. Appl. Phys. **104**, 024109 (2008).
[35] F. Rubio-Marcos, J. Romero, M. Martín-Gonzalez, and J. Fernandez, J. Eur. Ceram. Soc. **30**, 2763 (2010).
[36] K. Kakimoto, K. Akao, Y. Guo, and H. Ohsato, Jpn. J. Appl. Phys. **44**, 7064 (2005).
[37] M. Balkanski, R. F. Wallis, and E. Haro, Phys. Rev. B **28**, 1928 (1983).
[38] B. Jiménez and J. M. Vicente, J. Phys. D **31**, 130 (1998).
[39] N. Klein, E. Hollenstein, D. Damjanovic, H. J. Trodahl, N. Setter, and M. Kuball, J. Appl. Phys. **102**, 014112 (2007).
[40] P. Mahesh and D. Pamu, IOP Conf. Ser. Mater. Sci. Eng. **73**, 012141 (2015).
[41] P. S. da Silva, Jr., M. Venet, and O. Florêncio, J. Alloys Compd. **647**, 784 (2015).
[42] D. M. Evans, A. Schilling, A. Kumar, D. Sanchez, N. Ortega, M. Arredondo, R. S. Katiyar, J. M. Gregg, and J. F. Scott, Nat. Commun. **4**, 1534 (2013).
[43] G. L. Brennecka, J. F. Ihlefeld, J.-P. Maria, B. A. Tuttle, and P. G. Clem, J. Am. Ceram. Soc. **93**, 3935 (2010).